



An Infrared Temperature Measurement Method for Hot Stamping Parts Considering Directional Emissivity

Y. K. Gu^{1,2}, Z. H. Zhao^{1,2}, J. C. Wang^{1,2}, J. Y. Min^{1,2}, J. P. Lin^{1,2}(✉), P. X. He³,
L. Y. Shi³, and R. L. Wang³

¹ School of Mechanical Engineering, Tongji University, Shanghai 201804, China
jplin58@tongji.edu.cn

² Shanghai Key Laboratory for A&D of Metallic Functional Material, Tongji University,
Shanghai 200092, China

³ Jinan Aotto Automation Co., Ltd., Jinan 250306, China
he_puxuan@aotto.cn

Abstract. Infrared temperature measurement technology is widely used in the detection of surface temperature distribution of hot stamping parts. However, the accurate infrared temperature measurement for complex parts is still a problem due to the deviation of emissivity. In this study, a novel directional emissivity calibration was proposed for 22MnB5 hot stamping steel. A mathematical model considering directional emissivity was established and verified. Based on the projection and interpolation method, the directional emissivity is assigned to each pixel in the thermograph shot by infrared thermal imager. Finally, a high measurement precision within ± 25 °C was achieved for temperature measurement on 22MnB5 hot stamping parts.

Keywords: Directional emissivity · Infrared temperature measurement · Hot Stamping

1 Introduction

Hot stamping of 22MnB5 steel is an advanced forming process to improve the strength of automobile safety parts (e.g., B-pillar and bumper beam) and in favor of automobile lightweight [1, 2]. The temperature history of sheet metal during hot stamping determines the properties of the formed parts [3–5]. For example, the sheet metal temperature before mold closing should be higher than Ar3 to avoid the deterioration of mechanical properties caused by the transformation from austenite to ferrite [6, 7]. With the development of hot stamping technology, formed parts with tailored performance can be obtained through accurate temperature control [8]. Therefore, it is of great significance to obtain the sheet metal temperature with efficiency and accuracy for the quality control of formed parts.

In China, more than 300 hot stamping production lines have been equipped with infrared thermal imagers for temperature measurement of 22MnB5 sheets. The key to

improve the accuracy of the measurement depends on the appropriate emissivity of 22MnB5 [9]. However, it is difficult to accurately calibrate the emissivity of 22MnB5 during hot stamping due to several influence factors [10]. For hot stamping parts with complex surfaces, the observation angle significantly affected the calibration of emissivity. The emissivity of an object in different directions is not a fixed value, which is defined as directional emissivity [11, 12]. Although directional emissivity of certain materials (e.g., aluminum [13]) has been studied, the effect of observation angle on the emissivity of 22MnB5 steel with Al-Si coating before and after stamping is still unclear. Besides, the temperature measurement method considering directional emissivity of 22MnB5 during hot stamping has not been reported.

This study focused on obtaining accurate surface emissivity of hot stamping steel 22MnB5. Firstly, a calibration experiment of emissivity of 22MnB5 steel under different observation angles was conducted. To control the consistency of oxidation degree, each sample experienced the same temperature history as in the hot stamping process temperature history. After that, two mathematical models of directional emissivity were established at 730 °C and 220 °C. Then, an innovative method was proposed to assign the accurate emissivity to each pixel of the thermograph shot by infrared thermal imager. Finally, this proposed calibration method of directional emissivity was applied to the temperature measurement of an industrial hot stamping part, and a high measurement precision was obtained.

2 Experiment and Results

2.1 Material and Setup

2-mm-thick 22MnB5 sheets with 40 μm hot-dipped Al-Si coating were used in this work. All samples were prepared by wire cutting and the final size was 100 \times 100 mm. A commercial infrared thermal imager was used to calibrate the emissivity. The field angle of the imager was 90° \times 64° and $\text{FOV}/f = 7.7$ mm, where f was the focal length. The resolution of the imager was 640 \times 480.

2.2 Experimental Procedure

A K-type thermocouple was spot-welded at the center of the sample. This temperature history is presented in Fig. 1, which is an actual process of a production line. First, the sample was heated over its austenitizing temperature at 750 °C and kept heating until the total heating time reached 5 min in a muffle furnace. The sample was then placed at ambient condition for cooling, which is to simulate the temperature decrease during the transfer of sheet metal from the roller furnace to the press. When the surface temperature of the sample dropped to 730 °C, the first emissivity calibration was conducted. After that, the sample was cooled by high-speed nitrogen gas flow to simulate the quenching process in mold. When the sample temperature continuously decreased to 220 °C, the emissivity of the sample was calibrated again. Then, the procedure above was repeated by changing the observation angle.

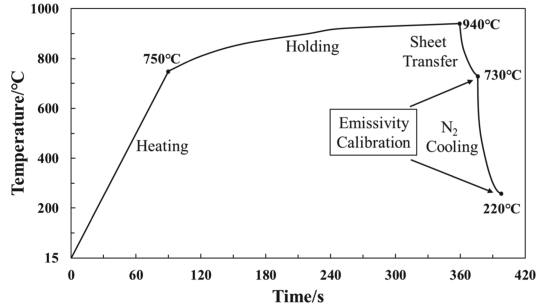


Fig. 1. Diagram of temperature variation during hot stamping of 22MnB5 steel.

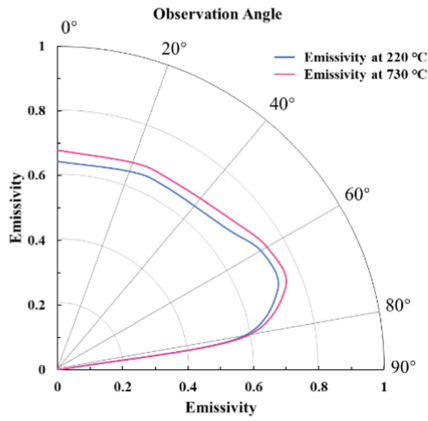


Fig. 2. Emissivity at different observation angles.

2.3 Experimental Results and Emissivity Modeling

Emissivity at 730 °C and 220 °C first increased and then decreased as indicated in Fig. 2. The maximum value of emissivity can be found at 60° or 70°. The emissivity at 730 °C is higher than that at 220 °C, and this was explained by the change of Al-Si coating on the sample surface [14].

In order to calculate the emissivity at arbitrary angles, a phenomenological model of emissivity ε_T and observation angle α was established by 5th-degree polynomial fitting. The emissivity model was shown in Eq. (1), in which the value of each coefficient and *R-square* values are listed in Table 1.

$$\varepsilon_T(\alpha) = p_1\alpha^5 + p_2\alpha^4 + p_3\alpha^3 + p_4\alpha^2 + p_5\alpha + p_6 \quad (1)$$

Table 1. Coefficients and *R-square* values of polynomial fitting function.

Model	p1	p2	p3	p4	p5	p6	R-square
E ₂₂₀ (α)	-2.20E-09	3.51E-07	1.89E-05	4.15E-04	-2.75E-03	0.646	0.9995
E ₇₃₀ (α)	-2.11E-09	3.28E-07	-1.68E-05	3.42E-04	-2.95E-03	0.679	0.9999

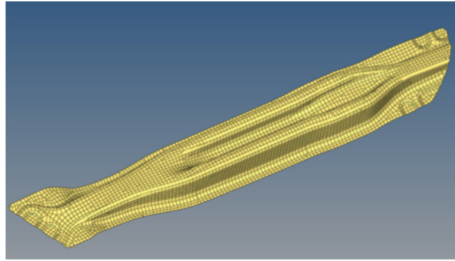


Fig. 3. Surface discretization by gridding method by taking a bumper beam as an example.

3 Extraction of Observation Angles on Complex Part Surface

3.1 Surface Discretization by Elements Meshing

In order to extract the observation angle of each point on the part surface, a surface discretization was compulsory. As presented in Fig. 3, the surface of the bumper beam has meshed with shell elements. Then the normal vector of each element’s center \vec{n}_i , and the direction vector pointing to the lens center of the imager \vec{v}_i was derived. Therefore, the observation angle of each element’s center α_i can be calculated by Eq. (2).

$$\alpha_i = \arccos \frac{\vec{n}_i \cdot \vec{v}_i}{|\vec{n}_i| \cdot |\vec{v}_i|} \tag{2}$$

3.2 Coordinate Transformation

The key optical component of an infrared thermal imager is its focal plane array (FPA) sensor. The radiation emitted by the object was imaged on the focal plane after being converged by the lens. This principle is illustrated schematically in Fig. 4. Therefore, a projection method was used to transform the coordinates of elements center on the part surface from three-dimensional space to two dimensions in a thermograph.

As presented in Fig. 4, the center of the imager lens (Point O) was supposed to be the origin. A projection plane perpendicular to the axis of the imager was determined. The distance between the plane and origin was set to 1 for the convenience of calculation. $P_i(x_i, y_i, z_i)$ is a point on the surface of the bumper beam. It’s easy to obtain coordinates of the projection $P_i^*(x_i^*, y_i^*, z_i^*)$ of P_i on the projection plane through the geometric relationship.

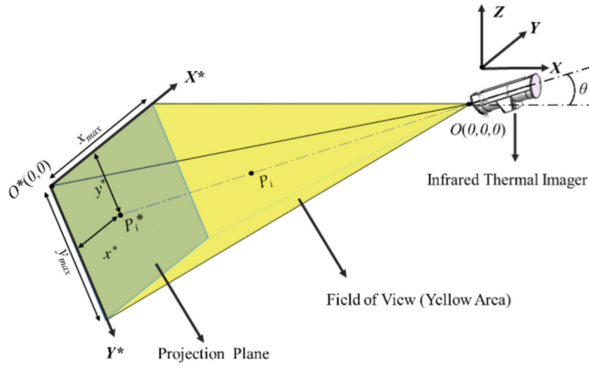


Fig. 4. Schematic diagram of the principle of projection method.

The FOV of the infrared thermal imager is a pyramid as shown in the yellow part in Fig. 4. The area where the pyramid intersects with the projection plane was visible to the imager as shown in light blue in Fig. 4. The length and width of this area are marked as x_{max} and y_{max} . If the horizontal and vertical field angles were marked as α_h and α_v respectively, x_{max} and y_{max} can be easily calculated according to the definition of field angle by Eq. (3).

$$x_{max} = 2 \tan \frac{\alpha_h}{2}, \quad y_{max} = 2 \tan \frac{\alpha_v}{2} \tag{3}$$

To match projected point coordinates with that in the thermograph, the top-left point was set as the new origin of coordinates ($O^*_{-x^*y^*}$ in Fig. 4) in the projection plane. The coordinates of the projected point $P_i^*(x_i^*, y_i^*, z_i^*)$ in the new system were calculated, and then the dimension of the coordinates can be reduced. That was, the coordinates in space can be transformed into plane coordinates.

From the geometric relationship, coordinates of new origin O^* under system O_{-xyz} can be easily obtained:

$$O^*(x_0^*, y_0^*, z_0^*) = \left(-\frac{y_{max}}{2} \sin\theta - \cos\theta, -\frac{x_{max}}{2}, \frac{y_{max}}{2} \cos\theta - \sin\theta \right) \tag{4}$$

where θ ($0^\circ < \theta < 90^\circ$) in Eq. (4) is the pitch angle of the imager, which should be measured after the imager was fixed. Next, calculate the distance from the point P_i^* to the new coordinate axes Y^* and X^* , that was, the horizontal and vertical coordinate values of P_i^* in the new coordinate system:

$$P_i^* = \left(y_i^* - y_0^*, \frac{x_i^* - x_0^*}{\sin\theta} \right) \tag{5}$$

The visualization process of coordinate transformation is shown in Fig. 5a and 5b.

Lastly, the coordinate values were scaled by the scaling factor k to match the real resolution (i.e., pixel coordinates) of the thermograph:

$$k = \frac{r_x}{x_{max}} = \frac{r_y}{y_{max}} \tag{6}$$

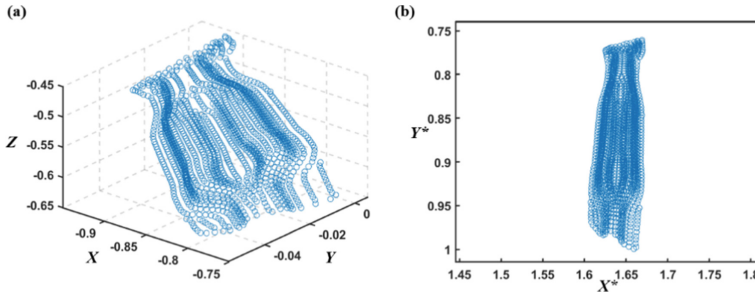


Fig. 5. Visual process of coordinate transformation: (a) The projected points P_i^* in system $O\text{-}xyz$, (b) The projected points P_i^* in system $O^*\text{-}x^*y^*$.

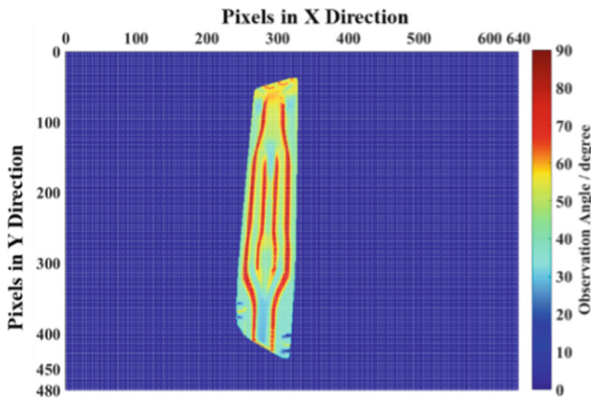


Fig. 6. Observation angle contour of the bumper beam after interpolation.

where r_x and r_y in Eq. (8) were the horizontal and vertical resolution of the imager. After that, the coordinate of P_i was transformed into the two-dimensional coordinate system in the thermograph, and the rescaled points were marked as $P_{s,i}^*(x_{s,i}^*, y_{s,i}^*)$.

3.3 Calculation of Observation Angle Matrix

The observation angle of each point on the bumper beam surface and its coordinates in the thermograph had been obtained. The observation angle and the coordinates are in one-to-one correspondence, i.e., $\alpha_i = f(x_{s,i}^*, y_{s,i}^*)$. The pixels of the thermograph can be regarded as an arrangement by grids. However, the coordinates of grids were integers while both $x_{s,i}^*$ and $y_{s,i}^*$ were not. Therefore, a multivariate interpolation method is used to query the angle value of each pixel. The interpolation results were shown in Fig. 6. It was an observation angle matrix of a bumper beam with a dimension of 640×480 . Figure 6 vividly shows the observation angle distribution on the part surface when monitoring the bumper beam by an infrared thermal imager.

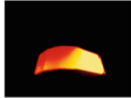








Position	Thermograph	Color map from calculation	Overlapped	Coincident Proportion
1				91.7%
2				97.2%
3				96.5%

Fig. 7. Coincident area proportion of thermograph and color map obtained by calculation.

3.4 A Verification of the Projection Method

To verify the consistency of the part profile between the thermograph shot by the imager and the color map like Fig. 6, two figures were overlaid together to calculate the proportion of the coincident area. A sheet metal part composed of four planes was selected as the observation object for verification. Validation experiments were carried out at three different observation positions. The results are shown in Fig. 7. The overlap proportion is not less than 91.7%, which is acceptable in engineering applications. The reason for incomplete overlap was the measurement error when measuring the relative position of the imager to the part.

4 Industrial Application

Through the emissivity model and the obtained observation angle of the part surface, each pixel in the thermograph can be assigned an accurate emissivity for temperature measurement. An example of engineering practice was given to show the improvement of temperature measurement accuracy.

Two emissivity distributions were assigned to parts in Fig. 8a and 8b respectively and the current temperature is 730 °C measured by thermocouples spot welded on the part surface. The emissivity can be regarded as a constant value when the surface temperature was in the range of 670 °C and 760 °C, which has been acknowledged in engineering practice [15, 16]. A fixed emissivity value of 0.61, which is widely accepted in industrial temperature measurement for boron steels, was assigned to the whole thermograph in Fig. 8a, and a measurement error of over 98 °C was obtained. Meanwhile, the method considering directional emissivity was used to process the same thermograph. In Fig. 8b, the measurement error was reduced to only 7 °C. This case proves that the temperature measurement method considering directional emissivity proposed in this study has more advantages than the traditional method. The comprehensive measurement error of this system can be controlled within ± 25 °C after repetitive verifications.

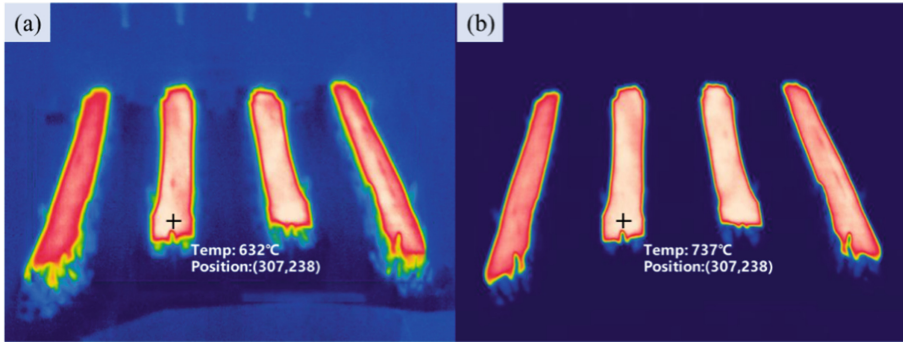


Fig. 8. Comparison of measurement accuracy at 730 °C: (a) Before optimization, (b) After optimization.

5 Conclusion

In this study, the directional emissivity of hot stamping steel 22MnB5 was accurately calibrated by simulating the temperature history in the hot stamping process. After that, an infrared temperature measurement method considering directional emissivity was proposed and an industrial application case was given.

- (1) Based on a rigorous emissivity calibration experiment by simulating the hot stamping temperature history, a mathematical model considering directional emissivity was established.
- (2) The calculated angle contours were obtained through projection and interpolation. The overlap ratios of part profiles between calculated angle contours and thermal images are not less than 91.7%.
- (3) The comprehensive measurement accuracy of the temperature measurement system considering directional emissivity proposed in this study can be controlled within ± 25 °C in industrial applications.

References

1. N. A. Z. Abdullah, M. S. M. Sani and M. S. Salwani, A review on crashworthiness studies of crash box structure, *Thin-Walled Structures* **153**, 106795 (2020).
2. H. Karbasian and A. E. Tekkaya, A review on hot stamping, *Journal of Materials Processing Technology* **210**, 2103 (2010).
3. L. Bao, W. Liu and B. Wang, Experimental investigation on partition controllable induction heating-hot stamping process of high-strength boron alloyed steel plates with designable temperature patterns, *Journal of Materials Research and Technology* **9**, 13963 (2020).
4. C. P. Couto, R. I. Revilla and R. Politano, Influence of austenitization temperatures during hot stamping on the local electrochemical behaviour of 22MnB5 steel coated with hot-dip Al-Si, *Corrosion Science* **190**, 109673 (2021).
5. O. Çavuşoğlu and A. G. Yılmazoğlu, Microstructural features and mechanical properties of 22MnB5 hot stamping steel in different heat treatment conditions, *Journal of Materials Research and Technology* **9**, 10901 (2020).

6. J. Y. Min, J. P. Lin, Y. A. Min and F. F. Li, On the ferrite and bainite transformation in isothermally deformed 22MnB5 steels, *Materials Science and Engineering A* **550**, 375 (2012).
7. T. H-R, J. B and M. B, Extension of a phase transformation model for partial hardening in hot stamping, *Journal of Machine Engineering* **18**, 87 (2018).
8. K. Wang, B. Zhu, L. Wang, Y. L. Wang and Y. S. Zhang, Tailored properties of hot stamping steel by resistance heating with local temperature control, *Procedia Manufacturing* **18**, 1087 (2018).
9. J. Dumoulin, J. Monchau and Y. Candau, Infrared emissivity measurements of building and civil engineering materials: A new device for measuring emissivity, *International Journal of Thermophysics* **35**, 1817 (2014).
10. C. M. Klassen, J. Emmert and K. J. Daun, Effect of coating thickness on the in-situ reflectance and surface roughness of Al-Si coated 22MnB5 steel, *Surface & Coatings Technology* **414**, 127100 (2021).
11. H. Jo, J. L. King and K. Blomstrand and K. Sridharan, Spectral emissivity of oxidized and roughened metal surfaces, *International Journal of Heat & Mass Transfer* **115**, 1065 (2017).
12. K. Yu, H. Y. Zhang, Y. Liu and Y. F. Liu, Study of normal spectral emissivity of copper during thermal oxidation at different temperatures and heating times, *International Journal of Heat and Mass Transfer* **129**, 1066 (2019).
13. B. Muller and U. Renz, Development of a fast fiber-optic two-color pyrometer for the temperature measurement of surfaces with varying emissivities, *Review of Scientific Instruments* **72**, 3366 (2001).
14. F. Li, M. Fu and J. Lin, Effect of cooling path on the phase transformation of boron steel 22MnB5 in hot stamping process, *The International Journal of Advanced Manufacturing Technology* **81**, 1391 (2015).
15. Y. Xu, K. Zhang and Y. Liu, Experimental investigation of spectral emissivity of copper-nickel alloy during thermal oxidation process, *Spectroscopy and Spectral Analysis* **09**, 2969 (2021).
16. K. Yu, R. Shi and H. Zhang, Experimental investigation of infrared spectral emissivity of pure tungsten, *Spectroscopy and Spectral Analysis* **01**, 107 (2020).

Open Access This chapter is licensed under the terms of the Creative Commons Attribution-NonCommercial 4.0 International License (<http://creativecommons.org/licenses/by-nc/4.0/>), which permits any noncommercial use, sharing, adaptation, distribution and reproduction in any medium or format, as long as you give appropriate credit to the original author(s) and the source, provide a link to the Creative Commons license and indicate if changes were made.

The images or other third party material in this chapter are included in the chapter's Creative Commons license, unless indicated otherwise in a credit line to the material. If material is not included in the chapter's Creative Commons license and your intended use is not permitted by statutory regulation or exceeds the permitted use, you will need to obtain permission directly from the copyright holder.

